

Effect of Manufacturing Conditions and Al Addition on Inclusion Characteristics in Co-Based Dual-Phase High Entropy Alloy



YONG WANG, YULONG LI, WEI WANG, HUI KONG, QIANG WANG,
JOO HYUN PARK, and WANGZHONG MU

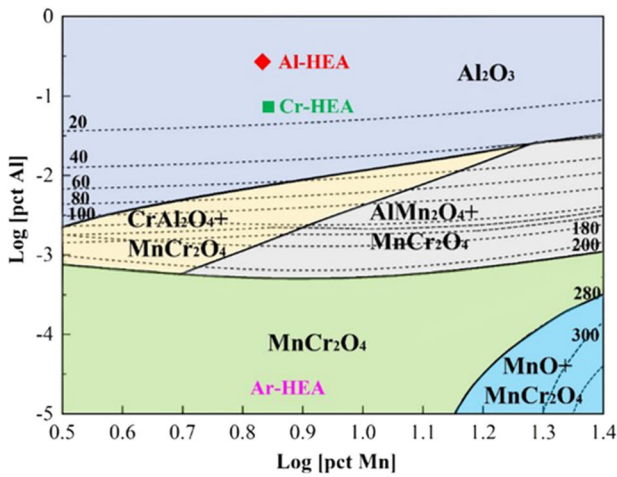
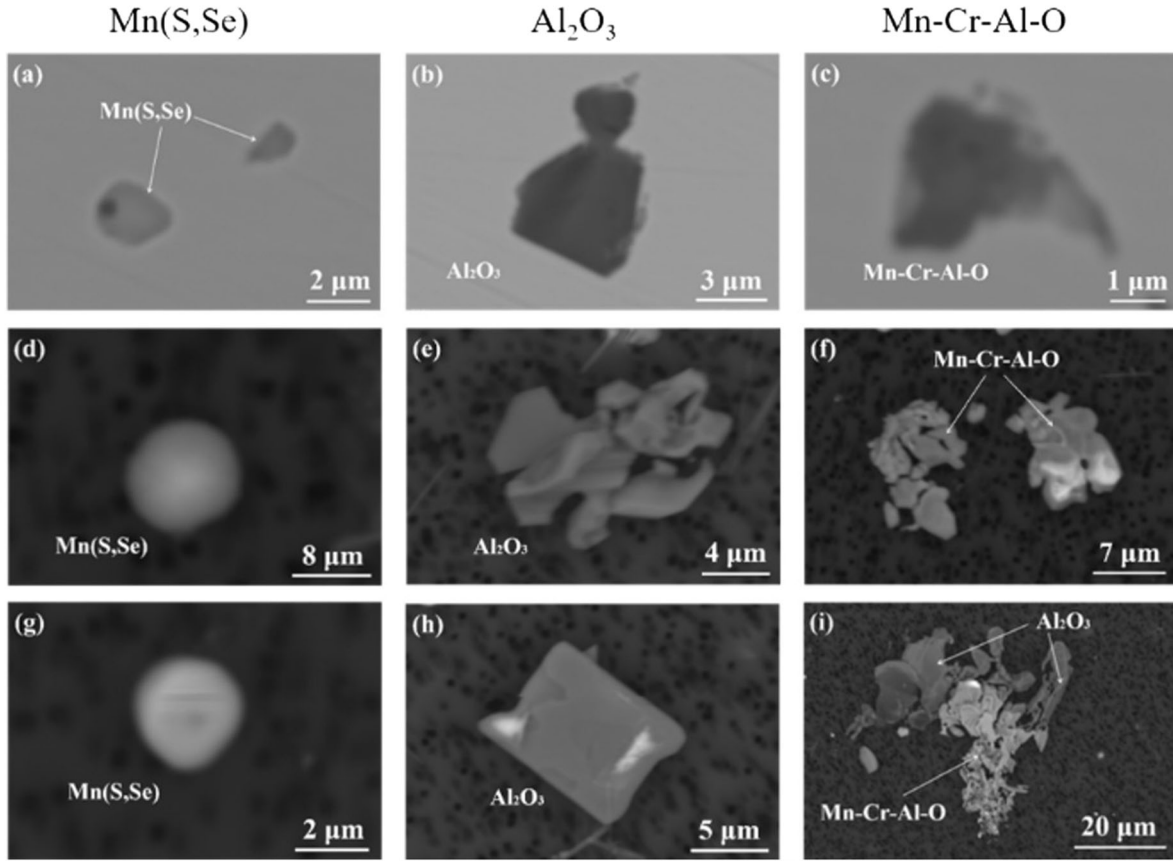
Three Co-based dual-phase high-entropy alloys (HEAs) were produced by different manufacturing conditions: arc-melting with Ar protection (Ar-HEA), vacuum induction melting in Al_2O_3 crucible (Cr-HEA) and vacuum induction melting with 0.5 at. pct Al (Al-HEA), which resulted in different levels of impurity elements and inclusion characteristics. The inclusions that precipitated in different HEA samples were investigated through an electrolytic extraction process and scanning electron microscopy-energy dispersive spectroscopy (SEM-EDS) characterization. The results showed that Mn(S,Se) inclusions were presented in all three alloys. MnCr_2O_4 inclusions were presented only in Ar-HEA, pure Al_2O_3 inclusions were presented in Cr-HEA and Al-HEA, and Mn–Cr–Al–O inclusions were also found in Al-HEA. Thermodynamic calculation software FactSage and Thermo-calc were used to predict the inclusion formations of the HEAs, which showed a good agreement with the experimental findings. The stable inclusions can transform from MnCr_2O_4 to $\text{Mn}(\text{Cr,Al})_2\text{O}_4$ and then to pure Al_2O_3 with the increase of Al content. The inclusions in Al-containing HEA are spinel or Al_2O_3 depending on the content levels of Al and O. It is proposed that the formation of spinel and Al_2O_3 inclusions can be avoided in liquid HEA when the O content is controlled to be very low, which can result in smaller-sized inclusions. Moreover, the calculated coagulation coefficient of spinel inclusions is close but lower than that of Al_2O_3 inclusions. The collision growth of inclusions was affected by a combination of physical parameters of HEA and inclusions as well as the inclusion size and amount.

YONG WANG is with the Key Laboratory for Ferrous Metallurgy and Resources Utilization of Ministry of Education, Wuhan University of Science and Technology, Wuhan 430081, P.R. China and also with the Department of Materials Science and Engineering, KTH Royal Institute of Technology, 100 44, Stockholm, Sweden. YULONG LI is with the Key Laboratory for Ferrous Metallurgy and Resources Utilization of Ministry of Education, Wuhan University of Science and Technology. WEI WANG is with the Department of Materials Science and Engineering, KTH Royal Institute of Technology and also with the Department of Chemical Engineering, Northeast Electric Power University, Jilin, 132012, P.R. China. Contact e-mail: wei6@kth.se HUI KONG is with the School of Metallurgical Engineering, Anhui University of Technology, Ma'anshan, Anhui, 243002, P.R. China. Contact e-mail: konghui@ahut.edu.cn QIANG WANG is with the Key Laboratory of Electromagnetic Processing of Materials (Ministry of Education), School of Metallurgy, Northeastern University, Shenyang 110819, P.R. China. JOO HYUN PARK is with the Department of Materials Science and Chemical Engineering, Hanyang University, Ansan, 15588, Korea. WANGZHONG MU is with the Department of Materials Science and Engineering, KTH Royal Institute of Technology and also with the Key Laboratory of Electromagnetic Processing of Materials (Ministry of Education), School of Metallurgy, Northeastern University. Contact e-mail: wmu@kth.se

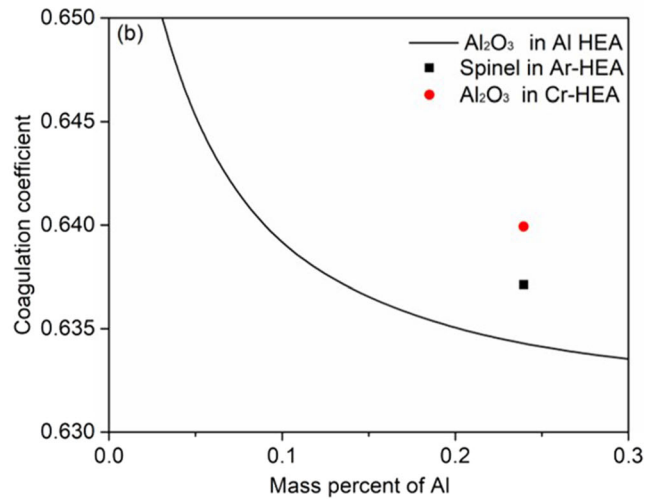
Manuscript submitted August 16, 2022; accepted April 4, 2023.

Article published online April 26, 2023

Characterization of inclusions in HEAs



Thermodynamics



Kinetics

<https://doi.org/10.1007/s11661-023-07049-1>
 © The Author(s) 2023

I. INTRODUCTION

HIGH entropy alloys (HEAs) can be defined as being composed of five or more elements in equimolar ratios or near equimolar ratios.^[1] For a long period of alloy design in the materials field, the basic principle is to add relatively small amounts of secondary elements to a primary element so as to improve the properties of materials. This new approach based on mixing together multiple principal elements in relatively high concentrations has attracted much attention since 2004.^[1,2] The quinary FeCoCrNiMn alloy was one of the first equiatomic HEAs reported to crystallize as a single-phase FCC solid solution. Subsequently, several important features of this alloy were revealed: tensile properties,^[3,4] dislocation structures and microstructural evolution,^[3,5] fatigue behavior,^[6,7] and creep behavior.^[8]

Besides, non-metallic inclusion (NMI) is another important issue which can affect the final mechanical and chemical properties of HEA alloys. Recently, some research has focused on the inclusion characterization in HEAs. Our recent work showed that MnCr₂O₄ oxide was the stable inclusion in the non-equiatomic CoCrMnNi and FeCoCrNiMn alloys prepared by an arc-melting method, while Cr₂O₃ was the main stable inclusion in the CoCrFeNi alloy. Moreover, MnCr₂O₄ had a higher agglomeration potency than Cr₂O₃.^[9] Choi *et al.*^[10] reported three different types of inclusions: Mn–Cr–Al oxide, Mn(S,Se), and mixed type with a Mn–Cr–Al oxide core surrounded by a Mn(S,Se) shell in an equiatomic FeCoCrNiMn alloy produced by a vacuum induction melting (VIM) method and the tensile properties of the HEA decreased as the number density of NMI increased. Livacoli *et al.*^[11] reported that MnS, Cr-based carbides, and oxides of Al and Si were formed from the impurities such as O, N, C, and S in CoCrFeNi and FeCoCrNiMn alloy made by the VIM method. Gludovatz *et al.*^[12] reported that small Mn-containing inclusions were difficult to avoid in normal melting practice when the alloys contained reactive elements in FeCoCrNiMn alloy. Choi *et al.*^[13] also proposed that atmospheric condition was an important factor to control the inclusion characteristics in FeCoCrNiMn alloy. They found that alloys melted under vacuum or using an inert gas atmosphere contained relatively large Al₂O₃ particles, while relatively fine MnCr₂O₄ particles rather than coarse Al₂O₃ inclusions were observed in the alloy melted under a purified Ar atmosphere followed by air exposure. Therefore, inclusions in HEAs are normally formed by the impurity elements from the raw materials and also affected by the manufacturing conditions during the production process.

In addition to the production process, a minor amount of Al has been added to different HEAs to enhance their mechanical properties.^[14–18] Except for the Al addition on alloy property, Al is a very reactive element and it can easily form harmful Al₂O₃ or AlN inclusions which will significantly reduce the quality of the alloy. Wong *et al.*^[19] reported that ~ 2 vol pct of

Al₂O₃ inclusions were found in Al_{0.3}CoCrFeNiMn_x produced through induction melting and casting in air. Al₂O₃ inclusions have been reported to provide nucleation sites for micro-cracks, which decrease the fatigue life of Al_{0.5}CoCrCuFeNi alloy.^[17] Kang *et al.*^[20] reported that a small amount of nano-sized Al₂O₃ inclusions (volume fraction less than 4 pct) was uniformly formed by *in-situ* reaction during the powder metallurgical process of Al_xCrNbVMo, and they contributed to the strength of the alloys by the Orowan strengthening mechanism. There has been little research focused on the systematic inclusion analysis in Al-added HEAs.

In this study, Co-based dual-phase HEAs (*i.e.*, Co_{47.5}Cr₃₀Fe_{7.5}Ni_{7.5}Mn_{7.5}-based alloys with different levels of Al contents) were manufactured *via* different methods, which had different impurity levels and Al contents. This alloy grade is selected due to its excellent mechanical property and corrosion resistance and potentially has a wide application, reported in References 21–23. Two- and three-dimensional (3D) morphologies, size distributions, number densities and chemical compositions of the NMIs and their formation mechanisms were discussed in different alloys under different conditions. Besides, the influence of small amount of Al addition associated with different manufacturing conditions on the inclusion characteristics will be investigated. This work aims to contribute to the application of ‘Inclusion/Precipitate Engineering’ concept^[24] in advanced HEAs.

II. MATERIALS AND METHODOLOGY

A. Alloys and Manufacturing Methods

Different HEA samples were manufactured in the following ways. Ar-HEA was prepared by arc-melting under Ar atmosphere (purity > 99.999 pct), detailed can be seen in Reference 9. Cr-HEA and Al-HEA samples were prepared in the vacuum induction melting furnace, pure metallic materials of Co, Cr, Fe, Mn, Ni and Al with a purity of over 99.95 pct were used. The vacuum chamber was evacuated to a pressure of approximately 5 Pa. Subsequently, the chamber was flushed with Ar (purity > 99.999 pct) three times, and finally each alloy was prepared using induction heating to a temperature of 1550 °C under vacuum condition and held for 5 min. Type-B (PtRh30-PtRh6) was used to control the furnace temperature. Samples were held and solidified in an Al₂O₃ crucible under vacuum condition. Detailed compositions as well as impurity elements of each sample can be seen in Table I. Cr-HEA and Al-HEA were designed based on a stoichiometric ratio of Co_{47.5}Cr₃₀Fe_{7.5}Ni_{7.5}Mn_{7.5}, using Al₂O₃ crucible leads to a trace amount of Al in the Cr-HEA. Furthermore, Al-HEA was designed to add a content of Al (0.5 at. pct) to investigate the influence of Al addition on inclusion characteristics.

Table I. Chemical Composition of Principal Elements and Impurity Level of the Three Alloys

Alloys	Alloy Elements, At. Pct (Wt Pct)						Impurity (Wt Pct)*		
	Co	Cr	Fe	Mn	Ni	Al	O	S	N
Arc-Melting Ar-HEA	bal	29.30 (27.01)	7.41 (7.34)	6.75 (6.58)	7.61 (7.92)	0	0.0193	< 0.003	< 0.01
Induction Melting Cr-HEA	bal	28.59 (26.34)	7.32 (7.24)	6.98 (6.79)	7.92 (8.24)	0.15 (0.07)	0.0158	0.004	0.01
Induction Melting Al-HEA	bal	28.28 (26.11)	7.58 (7.52)	6.83 (6.66)	7.98 (8.31)	0.5 (0.239)	0.0113	0.005	0.01

*C content is negligible to be detected in the alloys.

B. Characterization of Inclusions in Alloys Manufactured by Different Processes

Non-metallic inclusions were first analyzed in two-dimensional (2D) on polished cross-sections of the samples. Subsequently, the electrolytic extraction (EE) method was applied for the extraction of inclusion particles from the metal matrix. The following parameters were used for the EE method. The electrolyte was 10 pct AA (10 v/v pct acetylacetone, 1 w/v pct tetramethylammonium chloride-methanol), electric current was between 50 and 70 mA, voltage was between 3.5 and 4.2 V. The dissolved weight of the samples varied from 0.09 to 0.13 g. After the extraction, the solution containing inclusions was filtrated through a polycarbonate (PC) membrane film filter with an open pore size of 0.4 μm . Thereafter, the morphology and composition of the inclusions were characterized by scanning electron microscopes (SEM, JEOL JSM-7800F & Hitachi S3700N) equipped with the energy-dispersive X-ray spectroscopy (EDS) at an operating voltage of 15 kV. The equivalent diameter of a circle was used to present the inclusion sizes by measuring their real sizes on SEM images by Image software. The total observed area of the film filter for different samples varied from 1.88 to 4.78 mm^2 .

The number of inclusions per unit volume (N_V) was calculated using Eq. [1]:

$$N_V = n \cdot \frac{A_{\text{filter}}}{A_{\text{observed}}} \cdot \frac{\rho_{\text{alloy}}}{W_{\text{dissolved}}}, \quad [1]$$

where n is the number of inclusions in the appropriate size interval, A_{filter} is the area of the film filter with inclusions (1200 mm^2), A_{observed} is the total observed area on the film filter, ρ_{alloy} is the density of the alloy matrix, which was calculated by Thermo-Calc 2021b and $W_{\text{dissolved}}$ is the dissolved weight of the alloy during extraction.

III. RESULTS AND DISCUSSION

A. Morphology and Composition of Inclusions in Different Alloys

The representative 2D and 3D morphologies and compositions of inclusions in Ar-HEA are shown in Figure 1. A small amount of Mn(S,Se) inclusions were found occasionally on the film filters within a narrow

size range (< 3 μm) due to the quite low sulfur content (< 30 ppm), and they show spherical and globular shapes in 2D and 3D investigations, respectively. It was found that the Mn–Cr–O phases were the stable oxide inclusions in this alloy. Moreover, based on the EDS spectrums and the atomic ratio of Cr/Mn, it can be concluded that the Cr–Mn–O phase is MnCr_2O_4 spinel. This finding has been reported in Reference 9 to identify the inclusion phase. Besides, they show a polygonal morphology on cross-sections (Figure 1(b)) and their real octahedral shapes can clearly be seen on the film filters (Figure 1(e)), which is one of the typical morphologies of spinel structures. Except for the single MnCr_2O_4 particle, they can easily agglomerate to form clusters, which were more commonly found in this alloy (Figures 1(c) and (f)). The elemental mappings of one typical MnCr_2O_4 cluster can be seen in Figure 4(a), where Mn and Cr distribute homogeneously. Their agglomeration behavior has been discussed in detail elsewhere.^[9] Therefore, the MnCr_2O_4 spinel inclusion is the representative oxide present in $\text{Co}_{47.5}\text{Cr}_{30}\text{Fe}_{7.5}\text{Ni}_{7.5}\text{Mn}_{7.5}$ alloy when no other impurities are present in the materials, which shows good agreement with previous results in CoCrFeNiMn alloys.^[10,13] It should be noticed that almost all Mn(S,Se) inclusions were not found on the surface of the MnCr_2O_4 inclusions. In other words, there were no complex Mn(S,Se)– MnCr_2O_4 inclusions, where they presented as single Mn(S,Se) and MnCr_2O_4 inclusions.

The representative 2D, 3D morphologies and compositions of each type of inclusion in Cr-HEA are shown in Figure 2. The observed inclusions could be classified based on the chemical composition: Mn(S,Se), Al_2O_3 and mixed-phase with Al_2O_3 and Mn(S,Se). Most Mn(S,Se) inclusions show a longitudinal chain shape consisting of discontinuous parts on cross-sections (Figure 2(a)). However, their real dendritic or skeleton morphologies can clearly be seen by the EE method (Figure 2(d)), which has also been observed in steels.^[25] They were reported to be formed by a eutectic reaction ($L_1 \rightarrow \text{Fe} + \text{MnS}$ (s)) in the interdendritic spaces.^[26] In addition to the majority dendritic type Mn(S,Se) inclusions, a small amount of globular Mn(S,Se) inclusions (Figure 2(g)) were also found, which were formed by a monotectic reaction ($L_1 \rightarrow \text{Fe} + \text{MnS}$ (L_2)).^[26,27] These inclusions have been reported in previous works.^[10] Most Al_2O_3 inclusions show a spherical shape on cross-sections (Figure 2(b)) and a globular shape

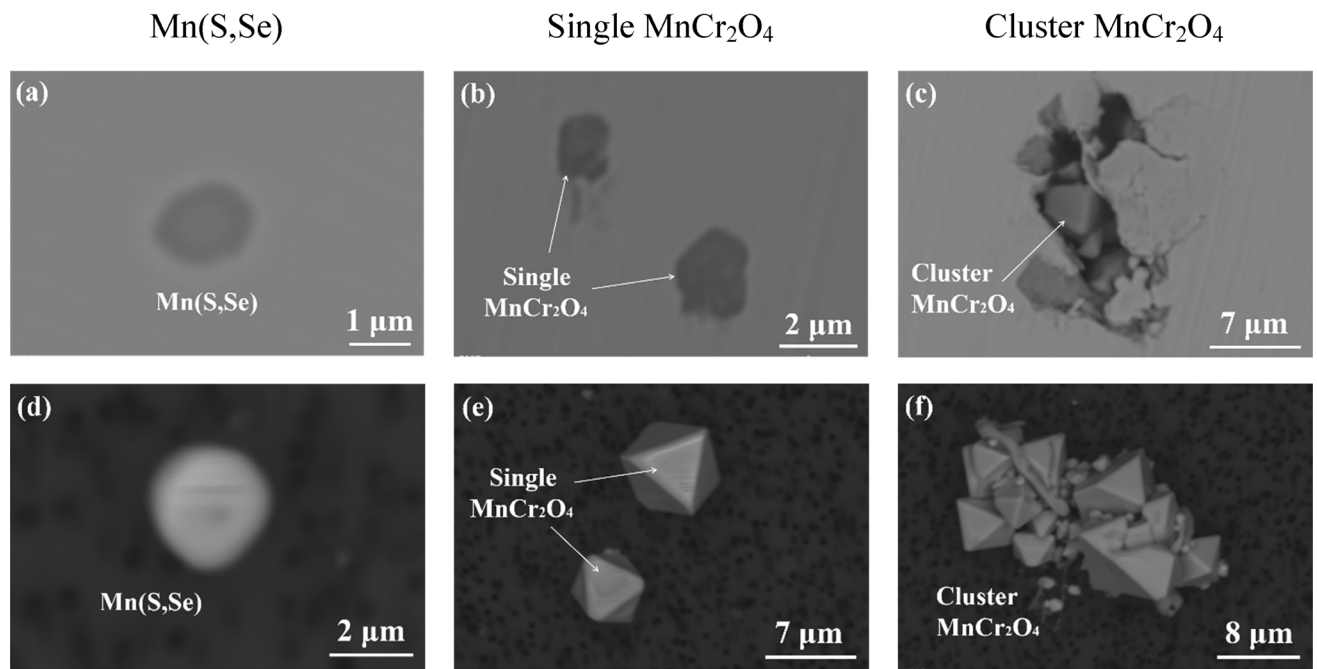


Fig. 1—Representative morphologies and chemical composition for different types of inclusions in Ar-HEA, (a) to (c) two-dimensional and (d) to (f) three-dimensional morphologies.

(Figure 2(e)) on film filters. Moreover, some irregular Al_2O_3 inclusions were also found and they were inclined to aggregate (Figure 2(h)). The third type of inclusion is a mixed one where Al_2O_3 inclusions are wrapped by dendritic $\text{Mn}(\text{S},\text{Se})$ inclusions. These inclusions can only be partially observed on cross-sections (Figure 2(c)) and their real morphology can clearly be seen after EE (Figures 2(f) and (i)). Their typical mappings by 3D observations are shown in Figure 4(b). It indicates that the EE method is preferable when investigating the complex inclusions compared to the 2D observations. $\text{Mn}(\text{S},\text{Se})$ inclusions are formed at the surface of the Al_2O_3 during the late stages of solidification. Due to the inclusion agglomeration, they were observed in sizes much larger than the other types of inclusions.

The typical 2D, 3D morphologies and compositions of inclusions in Al-HEA are shown in Figure 3. A large number of spherical and globular $\text{Mn}(\text{S},\text{Se})$ were found in this alloy (Figures 3(a), (d), (g)), which is similar to that in Ar-HEA. In terms of oxides, the majority type is irregular Al_2O_3 inclusion (Figures 3(b), (e), (h)). Similarly, they present as single particles, as well as clusters and their elemental mappings, can be seen in Figure 4(c). Agglomerated Mn–Cr–Al–O oxide inclusions (Figures 3(c), (f)) or together with Al_2O_3 inclusion (Figure 3(i)) were also observed in this alloy. According to EDS spectrums and their compositions, they are closer to the MnAl_2O_4 spinel inclusions which mix with a small amount of MnCr_2O_4 inclusions. They both have the same spinel structure and easily form an ideal solid solution. The typical mappings of this type of inclusion

can be seen in Figure 4(d), where Al, Mn, Cr and O show homogenous distributions.

To sum up, in combination with the 2D and 3D investigations, $\text{Mn}(\text{S},\text{Se})$ inclusions are present in all three alloys. Their precipitation is due to the tramp sulfur within the feed materials which is used to make these alloys. Usually S and Se are included in pure Mn during the aqueous electrolysis, and parts of S, Se are not completely removed during the production process. The difference is that they show dendritic or skeleton morphologies with larger size ranges in Cr-HEA, while they show globular shapes with small sizes in Ar-HEA and Al-HEA. Besides, $\text{Mn}(\text{S},\text{Se})$ inclusions were mainly found on the surface of oxides in Cr-HEA, but they were found in a single type in Ar-HEA and Al-HEA. This might be due to the different supersaturation degrees during the solidification process of these three alloys. Specifically, a spherical MnS is formed under uniform conditions of high supersaturation degree and when the size of a spherical crystal exceeds a critical value, complex shapes, such as dendritic would develop and form dendritic MnS.^[28,29] Regarding the oxide inclusions, only MnCr_2O_4 and pure Al_2O_3 inclusions are present in Ar-HEA and Cr-HEA, respectively. While in Al-HEA, pure Al_2O_3 inclusions present as the majority phases, and Mn–Cr–Al–O oxide inclusions are another stable phase. The formation of different types of oxide inclusions is closely related to the Al contents in these alloys, which is discussed in detail by thermodynamic calculation in Section III–C.

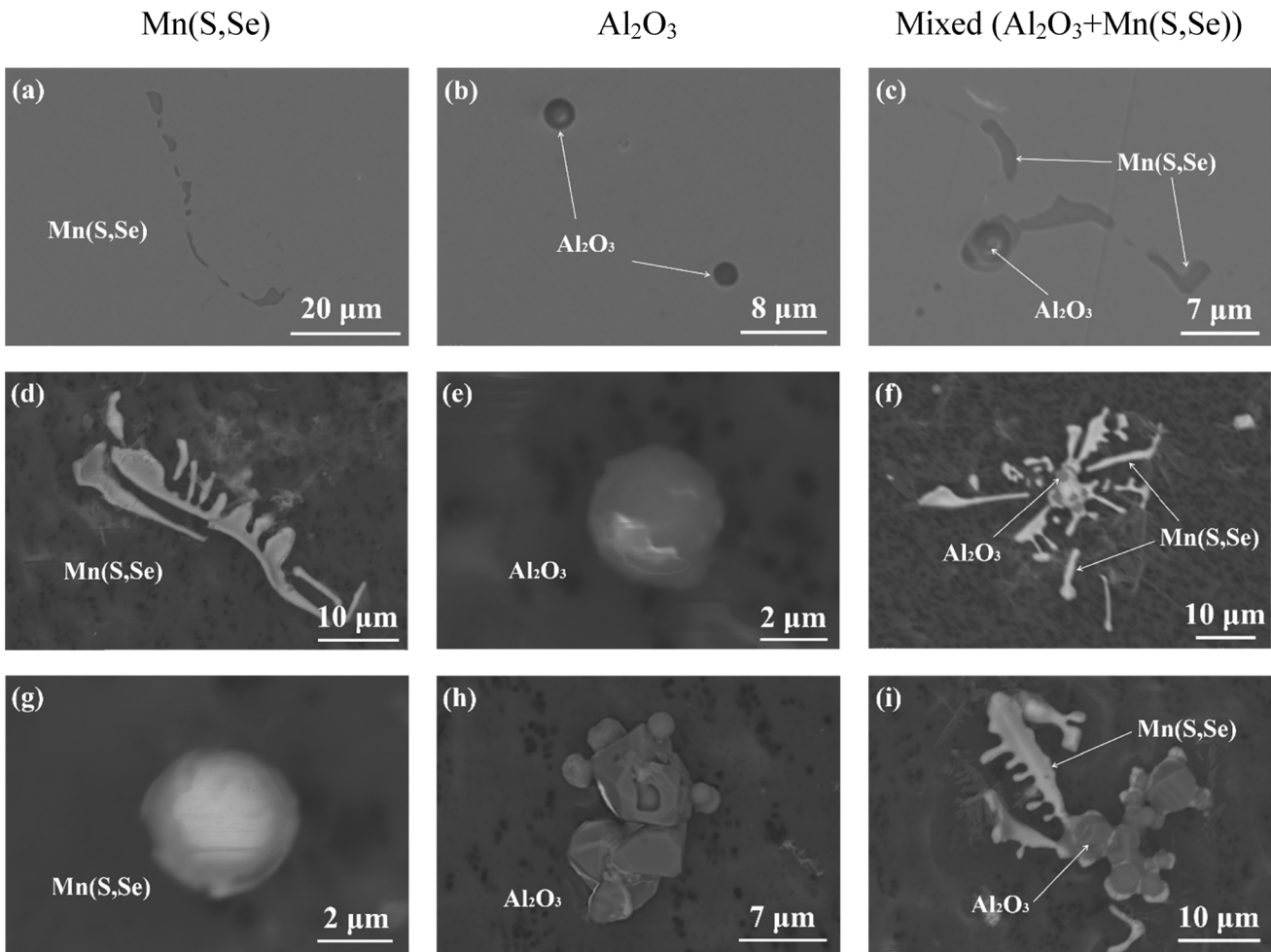


Fig. 2—Representative morphologies and chemical composition for different types of inclusions in Cr-HEA, (a) to (c) two-dimensional and (d) to (i) three-dimensional morphologies.

B. Size Distribution and Number Density of Inclusions in Different Alloys

The number and size distributions of inclusions in the three alloys were analyzed by the EE method, which showed a big advantage in measuring the accurate size of inclusions, especially for clusters.^[30] Figure 5 shows the total number density and particle size distributions of inclusions in the three alloys. It can be seen the size range of Mn(S,Se) inclusions (less than 3 μm) is much smaller than MnCr_2O_4 inclusions (1 to 18 μm), where the majority of MnCr_2O_4 inclusions have a size range of less than 6 μm in Ar-HEA (Figure 5(b)). The total number density of MnCr_2O_4 inclusions ($N_V = 17,508 \text{ mm}^{-3}$) is also larger than that of Mn(S,Se) inclusions ($N_V = 9882 \text{ mm}^{-3}$). In terms of Cr-HEA (Figure 5(c)), the Mn(S,Se) inclusions show the largest size ranges up to 32 μm as compared to other types of inclusions and the peak of the particle size distributions is at about 4 μm . In this alloy, the majority of Al_2O_3 inclusions show a size range of 1 to 8 μm but with the largest total number density ($N_V = 17,150 \text{ mm}^{-3}$). Moreover, the complex inclusions consisting of $\text{Al}_2\text{O}_3 + \text{Mn(S,Se)}$

have a much smaller number density ($N_V = 2088 \text{ mm}^{-3}$) and a wide size range (1 to 24 μm). When it comes to Al-HEA (Figure 5(d)), the size range and morphology of Mn(S,Se) inclusions are similar to those in Ar-HEA while it shows a much larger number density ($N_V = 22,330 \text{ mm}^{-3}$). This is followed by Al_2O_3 inclusions with a total number density of 8940 mm^{-3} . Even though the number density of Al_2O_3 inclusions is about half of that in Cr-HEA, they have much wider size ranges (1 to 20 μm) due to the formation of larger Al_2O_3 clusters. Therefore, the increase of Al content can greatly increase the size of Al_2O_3 inclusions. It should be noted that the Mn–Cr–Al–O inclusions present the largest size range up to 32 μm as compared to the other types of inclusions. Considering the alloy quality, the large-sized hard Al_2O_3 and Mn–Cr–Al–O inclusions in Al-HEA are more harmful than smaller-sized Al_2O_3 inclusions in Cr-HEA even though they have a much larger number density. The inclusion number density and agglomeration tendency are closely related to the impurity levels and also the physical properties of the liquid alloy, which are discussed in detail in Section III-D.

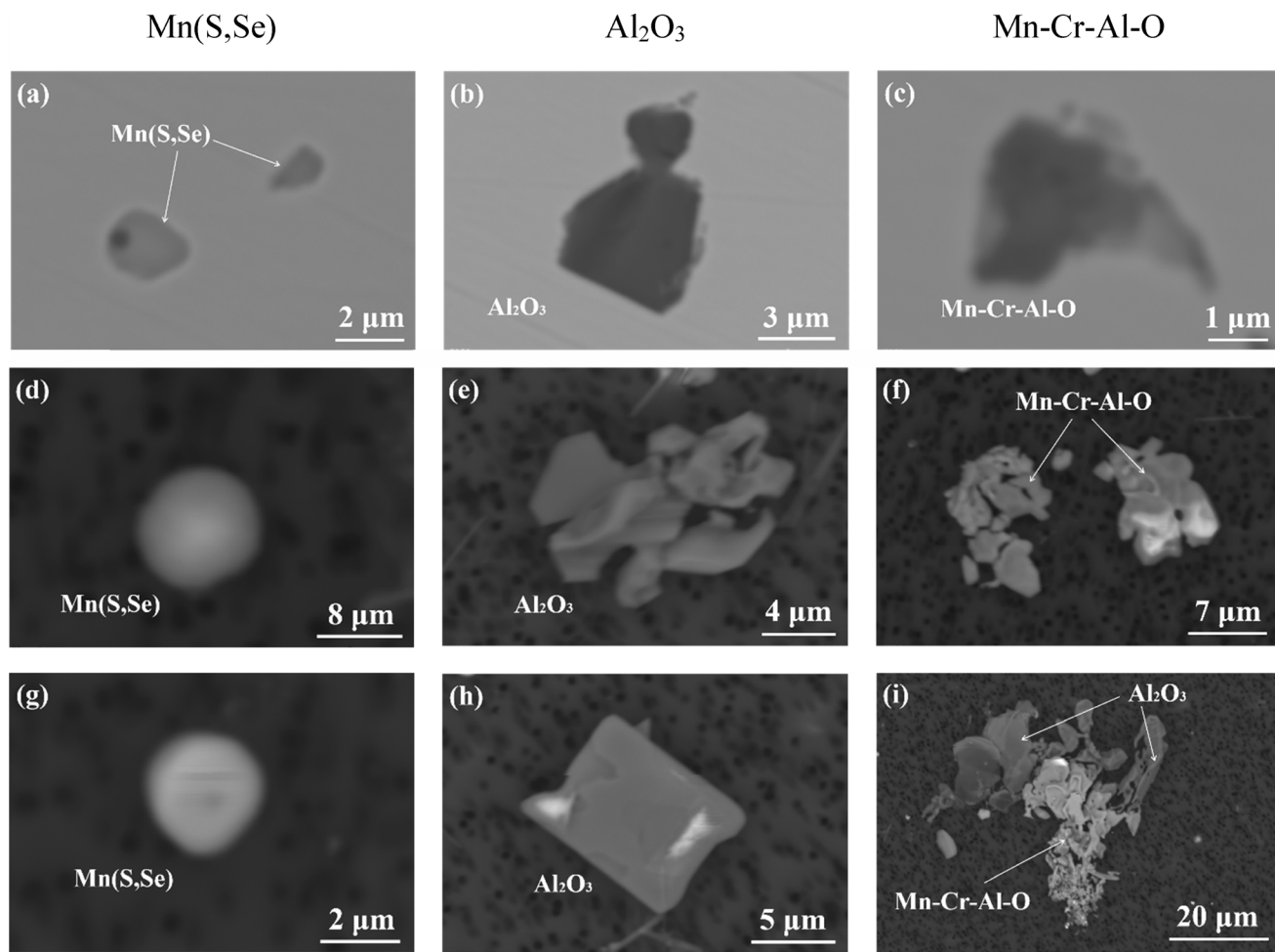


Fig. 3—Representative morphologies and chemical composition for different types of inclusions in Al-HEA, (a) to (c) two-dimensional and (d) to (i) -dimensional morphologies.

C. Thermodynamic Calculations of Inclusion Formation

To support the experimental findings, the equilibrium calculations of inclusion formation in the three HEAs were calculated by Thermo-calc 2021b^[31] with the TCFE11 database^[32] based on the chemical composition and the content of impurities in the HEA (Table I), the results are given in Figure 6. It is seen that the calculated liquid temperatures for the three alloys are slightly lower than 1400 °C. The predicted stable oxide inclusions in Ar-HEA are $MnCr_2O_4$ spinel, and those in Cr-HEA and Al-HEA are Al_2O_3 inclusions. Moreover, the amount of spinel inclusions is higher than those of Al_2O_3 inclusions due to the higher oxygen content in Ar-HEA. Besides, the formation temperatures of Al_2O_3 inclusions are higher than that of spinel inclusions. The amount of Al_2O_3 inclusions highly depends on the available Al and O contents. However, when the impurity element N is included, the formation sequence and amount of Al_2O_3 and AlN inclusions are another key issues regarding the inclusion control in Al-containing HEA. As can be seen that AlN inclusions are predicted to form below the solidus temperatures of Cr-HEA and Al-HEA. Therefore, they are not present in liquid HEA, and they were

not found in the experiment. The fact is that AlN forms at a low-temperature range in the equilibrium calculation which is far from the real experimental condition using air quenching during cooling. The formation and control of Al_2O_3 and AlN inclusions will be discussed in detail in another grade of HEA with much higher Al content elsewhere, where AlN inclusions can form in the liquid state.

In terms of sulfide, it is predicted to form in a solid HEA matrix during the solidification of HEA. It is interesting to note that (Mn,Co)S forms at the beginning of the solidification process, and it transforms to MnS in Cr-HEA and Al-HEA. (Mn,Co)S inclusions were not found in the experimental condition. As equilibrium calculation assumes that enough diffusion occurs in the solid phases by way of retaining an extremely low cooling rate. However, the equilibrium state usually cannot be reached in an actual experimental condition. The calculated results show a relatively good agreement with the experimental findings with the exceptions of the Mn-Cr-Al-O inclusions in Al-HEA, the possible reasons are discussed in the subsequent section.

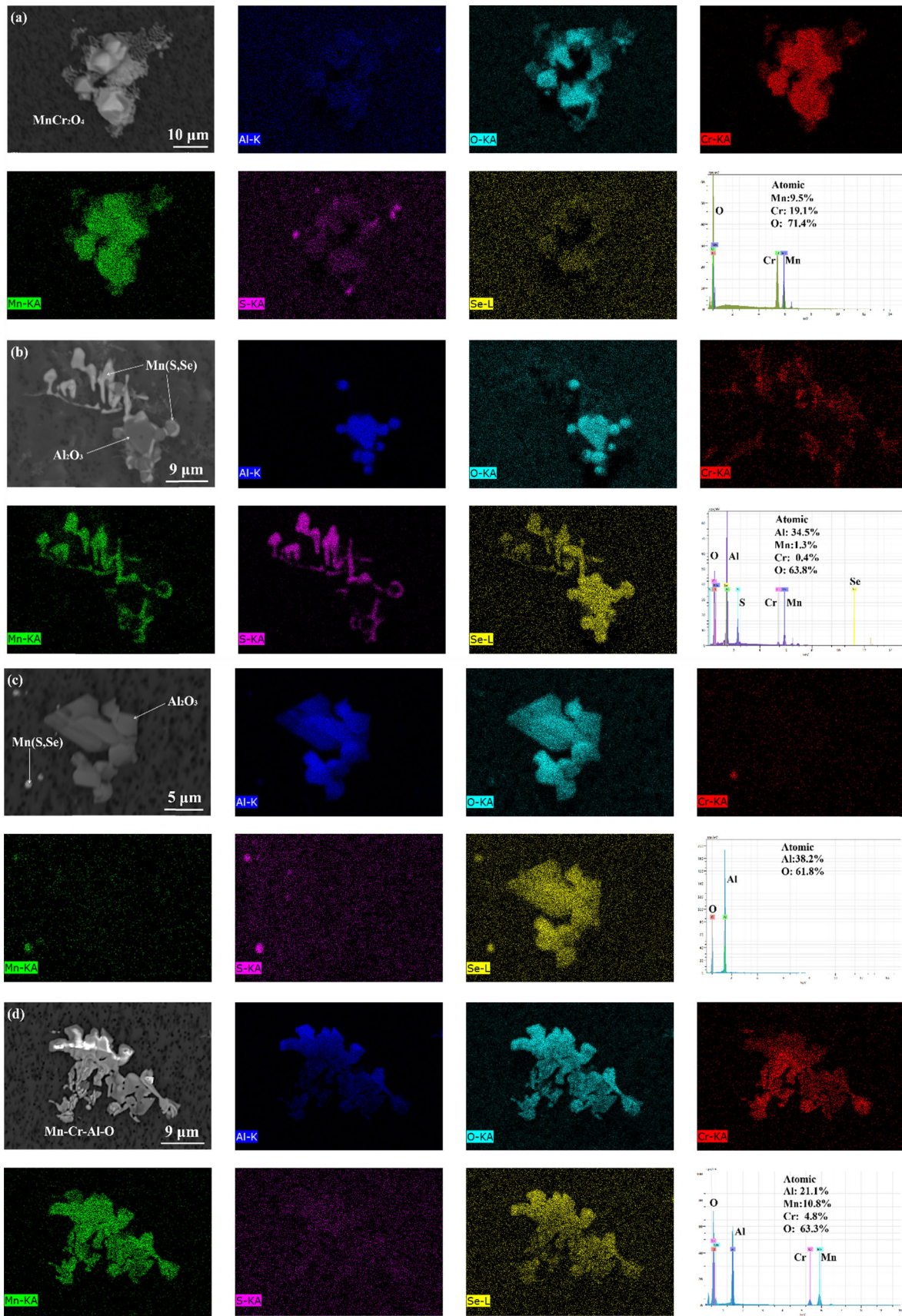


Fig. 4—Elemental mappings and EDS spectrums of typical inclusions in (a) Ar-HEA, (b) Cr-HEA and (c, d) Al-HEA.

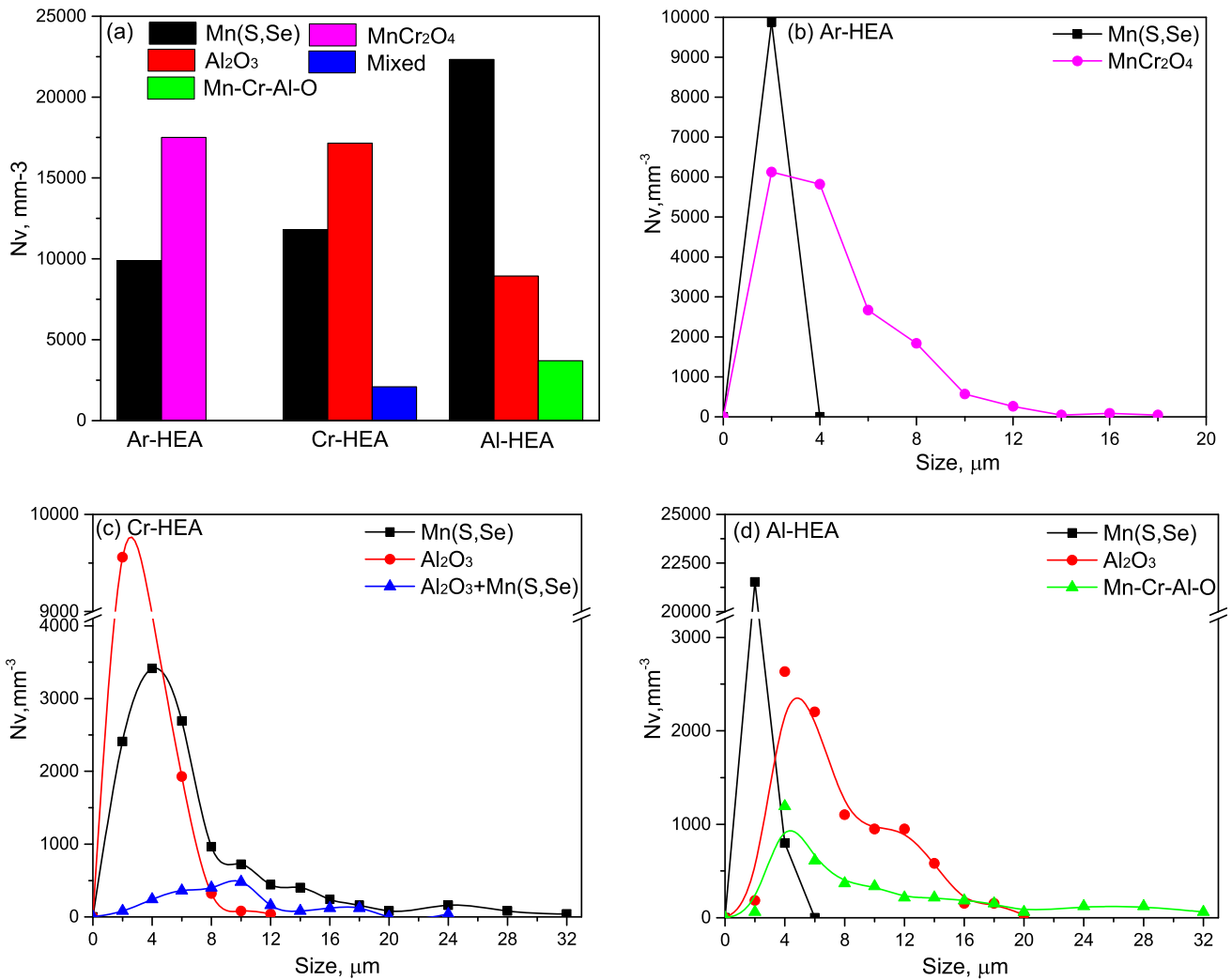


Fig. 5—The number density of inclusions in three alloys (a) and particle size distributions of different types of inclusions in (b) Ar-HEA, (c) Cr-HEA and (d) Al-HEA.

The stability diagram of different phases in the $\text{Co}_{47.5}\text{Cr}_{30}\text{Fe}_{7.5}\text{Ni}_{7.5}\text{Mn}_{7.5}$ HEA system at 1773 K (1500 °C) was calculated using the phase diagram module in FactSage 8.1 program with the databases of FactPS, FToxide and FSstel, as shown in Figure 7. Under the varied Al and Mn contents, different regions were predicted to form depending on the oxygen contents, namely Al_2O_3 , $\text{MnAl}_2\text{O}_4 + \text{MnCr}_2\text{O}_4$, $\text{CrAl}_2\text{O}_4 + \text{MnCr}_2\text{O}_4$, MnCr_2O_4 and $\text{MnO} + \text{MnCr}_2\text{O}_4$. The dashed lines (and numbers) represent the equilibrium oxygen concentration (ppm) in the liquid alloy. It is found that the stable inclusions transform with the increase of Al contents in the following order: $\text{MnCr}_2\text{O}_4 \rightarrow \text{Spinel} \rightarrow \text{Al}_2\text{O}_3$. The compositions of three different HEAs are given in Figure 7. No Al was detected in Ar-HEA, therefore it is located in the MnCr_2O_4 region by assuming an extremely low Al concentration. The compositions of Cr-HEA and Al-HEA are located in the Al_2O_3 region. These predicted results are in good agreement with the experimental results. This kind of phase stability diagram has been successfully applied in FeCoCrNiMn

alloy^[13] as well as different steels.^[33] In addition, it should be pointed out that the $\text{Al}_2\text{O}_3 + \text{spinel}$ dual region was not present in this stability diagram, which cannot explain the presence of different types of inclusions directly. The presence of aforementioned $\text{Mn}(\text{Cr,Al})_2\text{O}_4$ inclusions in Al-HEA might be due to the kinetic issue. Al-HEA includes a higher content of Al, partial Al transfers to form as a stable phase of Al_2O_3 , and the excess Al starts to form as the spinel and has not transferred to be Al_2O_3 yet. Detailed transformation kinetics of inclusion in the liquid HEA alloy will be performed in future study.

To better understand the effect of Al on inclusion formation, equilibrium calculations of stable phases were performed based on the composition of Cr-HEA under different Al contents, as shown in Figure 8. It is seen that spinel inclusions are the stable phases without any Al content, the amount of spinel inclusions first greatly increases with the increase of Al content and reaches a maximum value (Figure 8(a)). Thereafter, Al_2O_3 inclusions start to form where spinel inclusions significantly decrease and disappear. The amount of

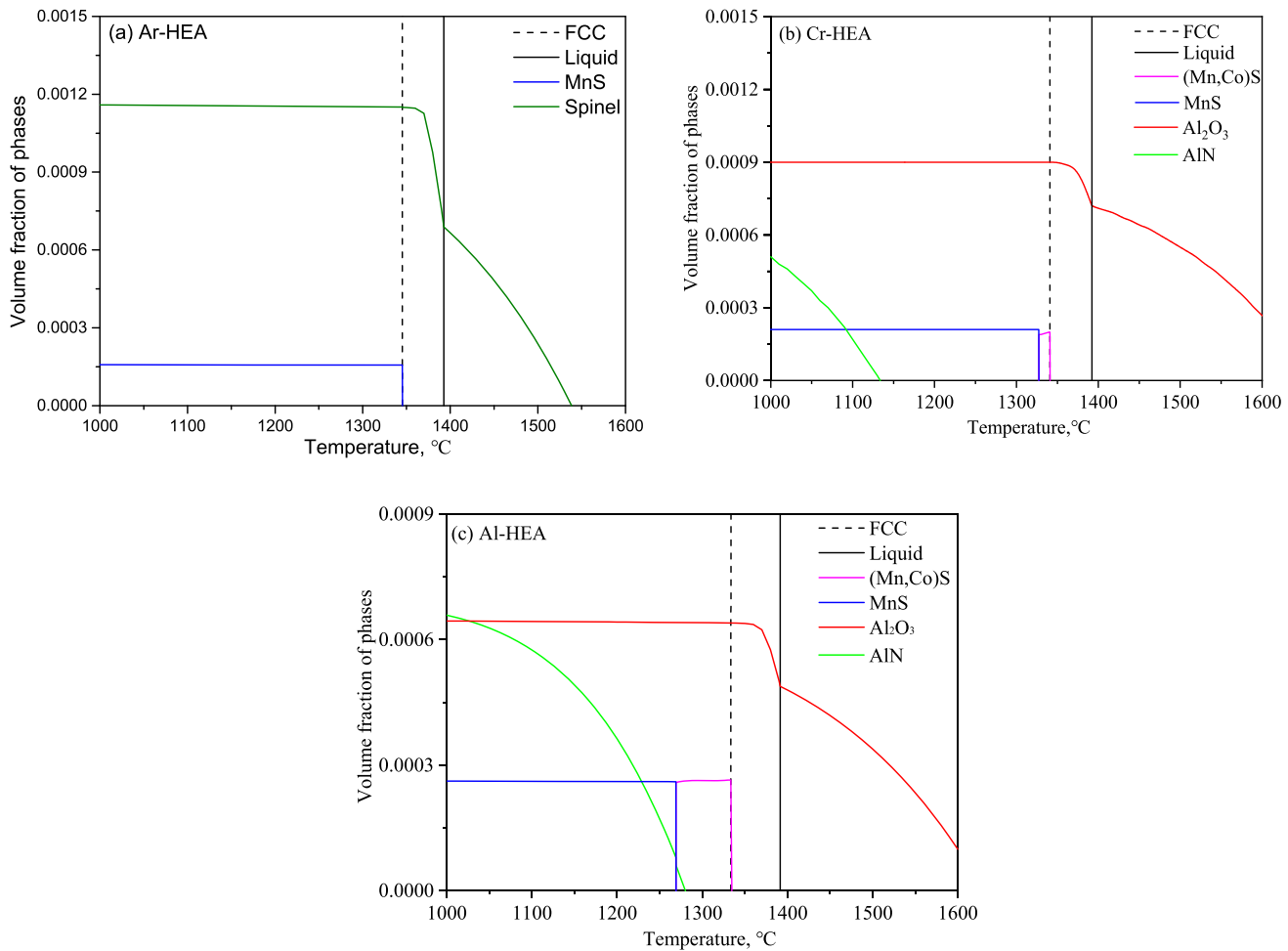


Fig. 6—Equilibrium calculations of phase formations in different samples (a) Ar-HEA, (b) Cr-HEA and (c) Al-HEA.

Al_2O_3 inclusions greatly increases at the beginning of their formation, and it slightly increases with the increase of Al content due to the limited oxygen. Moreover, the amount of element change in spinel inclusions is also presented in Figure 8(b). It is clearly seen that MnCr_2O_4 spinel inclusions are the stable phases when Al content is almost negligible, which fits well with the experimental results in Ar-HEA. With the increase of Al content, the MnCr_2O_4 spinel inclusions start to transform to $\text{Mn}(\text{Cr},\text{Al})_2\text{O}_4$ spinel inclusions. After the formation of Al_2O_3 inclusions, the amount of Al, Cr and Mn in $\text{Mn}(\text{Cr},\text{Al})_2\text{O}_4$ spinel decreases. This indicates that both spinel and Al_2O_3 can present within a certain Al concentration range. According to the thermodynamic calculation and composition analysis, $\text{Mn}(\text{Cr},\text{Al})_2\text{O}_4$ inclusions are commonly becoming to be homogeneous, but they also show a mixture of MnCr_2O_4 and MnAl_2O_4 inclusions. MnCr_2O_4 and MnAl_2O_4 were reported to easily form a solid solution at a temperature range from approximately 1773 to 1873 K^[33] due to their similar lattice parameters^[34] and the same cubic spinel structure. Moreover, the available O content can also result in the presence of both spinel and Al_2O_3 inclusions. The complex inclusions containing an Al_2O_3 core wrapped

by $\text{Mn}(\text{Cr},\text{Al})_2\text{O}_4$ inclusions were reported in FeCoCr-NiMn alloy.^[10]

To sum up, in a combination of experimental characterization and thermodynamic calculation, MnCr_2O_4 is the stable inclusion in $\text{Co}_{47.5}\text{Cr}_{30}\text{Fe}_{7.5}\text{Ni}_{7.5}\text{Mn}_{7.5}$ HEA. Moreover, the stable inclusions can transform from MnCr_2O_4 inclusions to $\text{Mn}(\text{Cr},\text{Al})_2\text{O}_4$ inclusions and then change to pure Al_2O_3 inclusions with the increase of Al content in the system due to the higher affinity between Al and O compared to those between Cr, Mn and O.

Based on above discussions, spinel or Al_2O_3 inclusions are unavoidable depending on different Al contents in $\text{Co}_{47.5}\text{Cr}_{30}\text{Fe}_{7.5}\text{Ni}_{7.5}\text{Mn}_{7.5}$ HEA. In addition to the type of inclusions, the amount and size of inclusions are also important issues controlling the quality of the HEA. The amount of these inclusions is closely related to the O content, which is discussed in detail here. It is well-known that inclusions can be divided into two groups, namely primary inclusions and secondary inclusions, where primary inclusions usually have larger sizes than secondary ones. Moreover, most secondary inclusions are formed during the solidification process due to decreasing thermodynamic solubility of oxygen in the HEA at lower temperatures, where inclusion size is

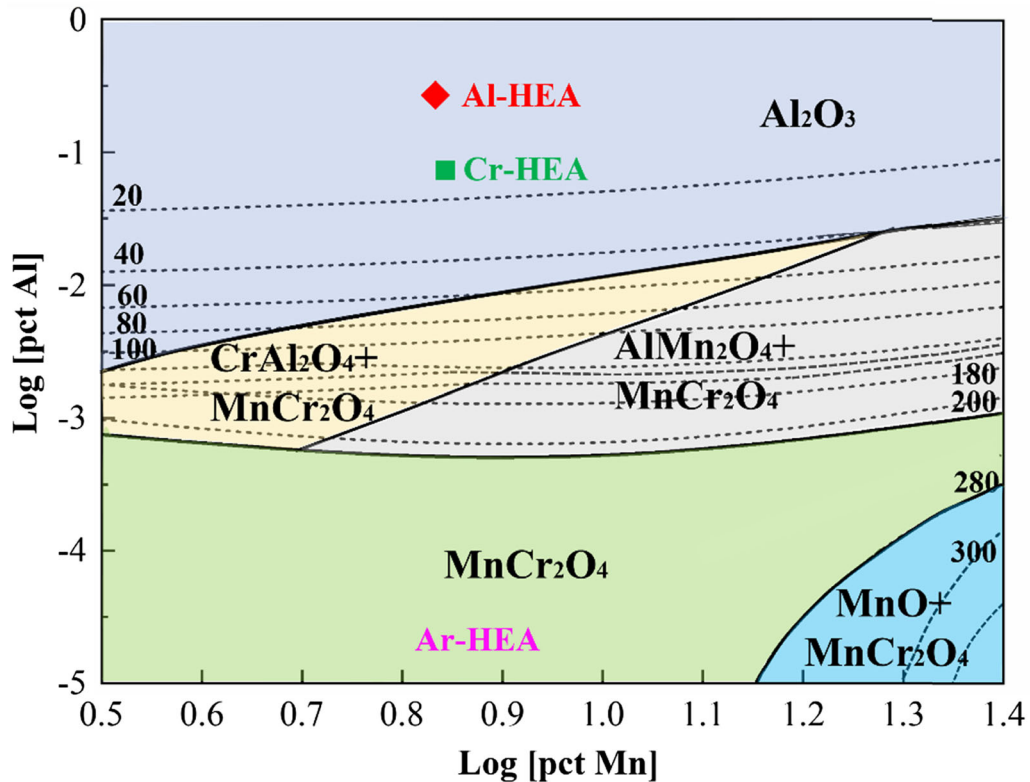


Fig. 7—Phase stability diagram of $\text{Co}_{47.5}\text{Cr}_{30}\text{Fe}_{7.5}\text{Ni}_{7.5}\text{Mn}_{7.5}$ HEA at 1773 K.

greatly affected by the cooling rate and chemical compositions of HEA (*i.e.*, diffusion rate of different elements).

To better control the spinel and Al_2O_3 inclusions, the effect of O content on the formation of these inclusions was evaluated using Thermo-calc 2021b, the results are given in Figure 9. It is seen in Figure 9(a) that the amount and the formation temperature of spinel inclusions increase with the increase of O content. Specifically, the spinel inclusions start to form in the mushy zone (temperature between T_s and T_l) of the HEA under the O contents of 20 and 50 ppm, and it forms above 1500 °C when the O content reaches about 200 ppm. This can be clearly seen in Figure 9(b), the spinel inclusions can only be formed when the O content is larger than 50 ppm at a temperature of 1400 °C. It suggests that by controlling the O content at a lower level (here less than 50 ppm), the spinel inclusions cannot form in liquid $\text{Co}_{47.5}\text{Cr}_{30}\text{Fe}_{7.5}\text{Ni}_{7.5}\text{Mn}_{7.5}$ HEA melt, which results in the decrease of the spinel inclusions.

A similar calculation was performed in the $\text{Co}_{47.5}\text{Cr}_{30}\text{Fe}_{7.5}\text{Ni}_{7.5}\text{Mn}_{7.5}$ HEA by considering the Al content of 0.01 pct, as shown in Figure 9(c). Under the O content of 20 ppm, Al_2O_3 inclusions form rather than spinel inclusions in the mushy zone. Similarly, the formation temperature of Al_2O_3 inclusions also increases with the increase of O content. It is found that Al_2O_3 inclusions form first and spinel inclusions can also form at a lower temperature when the O content increases to 80 ppm. However, spinel inclusions are only present at a certain

temperature range. Spinel and Al_2O_3 inclusions are stable inclusions when the O content is 100 ppm, whereas only spinel inclusions are formed when the O content is 200 ppm. This shows good agreement with the stability phase diagram of the inclusion formation in Figure 7. In addition, the effect of O content on inclusion formation was calculated under different Al contents at 1400 °C, as shown in Figure 9(d). It is found that Al_2O_3 and spinel inclusions cannot form in liquid $\text{Co}_{47.5}\text{Cr}_{30}\text{Fe}_{7.5}\text{Ni}_{7.5}\text{Mn}_{7.5}$ HEA melt when the O content is kept at a lower content (*e.g.*, 20 ppm O). The stable inclusions transform from spinel inclusions to Al_2O_3 inclusions with the increase of Al content. Besides, the amount of inclusions increases as the O content increases.

Based on these findings and previous works,^[9,11] the stable inclusions in HEA system greatly depend on the activity of the element and the impurities (O, N, S *etc.*). To sum up, the stable oxides in $\text{Co}_{47.5}\text{Cr}_{30}\text{Fe}_{7.5}\text{Ni}_{7.5}\text{Mn}_{7.5}$ HEA are MnCr_2O_4 spinel inclusions, and those in Al-containing HEA can be spinel or Al_2O_3 inclusions depending on Al content as well as O content. Under the same level of O content, Al_2O_3 inclusions are more easily formed compared to spinel inclusions. The spinel inclusions can be formed below the liquid temperature of the HEA when controlling the O content less than 50 ppm in $\text{Co}_{47.5}\text{Cr}_{30}\text{Fe}_{7.5}\text{Ni}_{7.5}\text{Mn}_{7.5}$ HEA, and also the formation of Al_2O_3 inclusions in liquid HEA can be avoided at a lower O content. As a result, the size and amount of inclusions can be kept at a small level. It should be noted that these results are only based

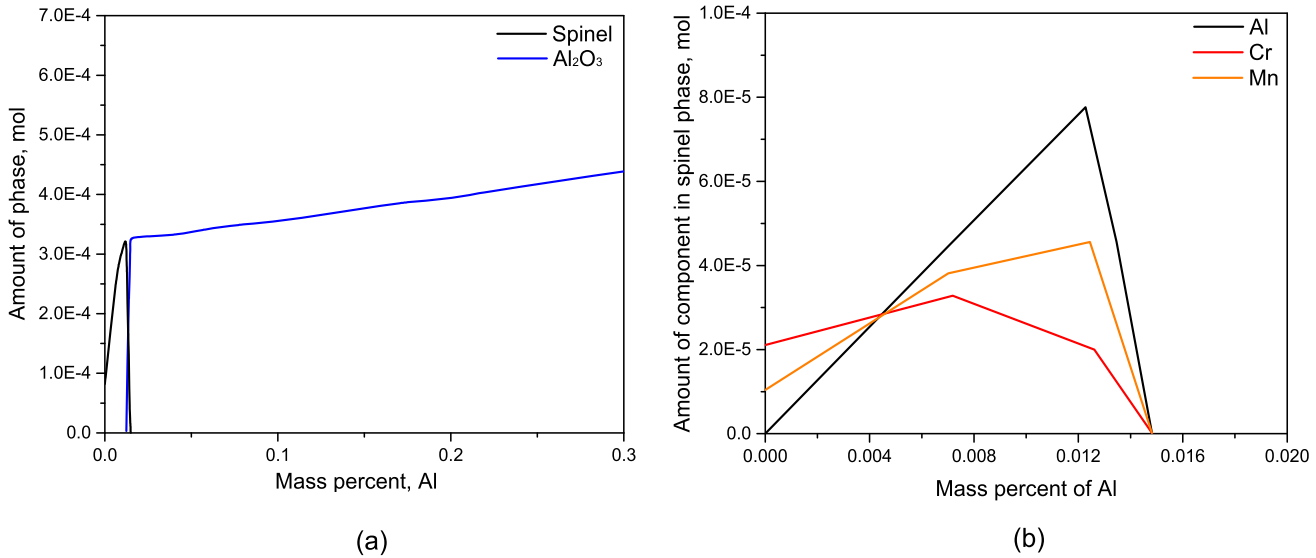


Fig. 8—Effect of Al content on (a) the transformation of inclusions and (b) the composition changes of spinel inclusions in $\text{Co}_{47.5}\text{Cr}_{30}\text{Fe}_{7.5}\text{Ni}_{7.5}\text{Mn}_{7.5}$ HEA.

on thermodynamic calculations, further experimental validation needs to be performed to verify this to better control the inclusion characteristics in CoCrFeNiMn HEA.

D. Agglomeration Potency of Different Types of Inclusions

Based on the morphologies of different inclusions, spinel and Al_2O_3 were easily formed clusters due to the inclusion agglomerations. The agglomeration behavior of different inclusions can attribute to the physical parameters of inclusions and melt, *i.e.*, interfacial energy, density, viscosity. Coagulation coefficient, α , which represents the agglomeration potency of inclusions in the liquid entropic alloys, is calculated using Eq. [2].^[35]

$$\alpha = 0.727 \left[\mu r_i^3 \sqrt{\frac{\rho_{\text{HEA}} \varepsilon}{\mu}} / 24\pi a^2 \gamma_{IM} \right]^{-0.242}, \quad [2]$$

where ε is the turbulent energy dissipation rate ($0.01 \text{ m}^2/\text{s}^3$), r_i is the radius of the inclusion particle (m), a is the ionic radius ($2.8 \times 10^{-10} \text{ m}$ for Al_2O_3).^[35] μ is the dynamic viscosity of alloy, ρ_{HEA} is the density of the liquid HEA, γ_{IM} is the interfacial energy (J/m^2) between the inclusion particle and the liquid HEA, these parameters were calculated by Thermo-Calc 2021b with the TCNI11 database due to the absence of physical parameters in the HEA system, the same method has been applied in Co-based dual-phase HEA.^[9]

Figure 10 shows the calculated coagulation coefficient of different inclusions in different alloys at $1500 \text{ }^\circ\text{C}$ with inclusion sizes of 2, 5, and $10 \text{ }\mu\text{m}$. It can be seen that the coagulation coefficients of spinel inclusions in Ar-HEA is higher than that of Al_2O_3 in Al-HEA. Besides, both the coefficients of spinel and Al_2O_3 inclusions are smaller than that of Al_2O_3 in Cr-HEA. The calculated

tendency does not show a good agreement with the experimental observations of the inclusion size distributions of spinel and Al_2O_3 inclusions. It should be pointed out that the calculated coefficients are close to each other, which is due to the similar HEA densities and similar interfacial energies between inclusions and HEA melt (Figure 10(a)). The coagulation coefficients of different inclusions decrease with the increase of inclusion size, which indicates that smaller inclusions are more easily to agglomerate. Also, the precipitation of MnS inclusions on the surface of Al_2O_3 inclusions can affect the size of agglomerated Al_2O_3 inclusions. The different number density of inclusions can also result in the different collision growth of inclusions.

In addition, it is found that the interfacial energy between Al_2O_3 and Al-HEA varies with the Al amount, which results in different numbers of Al_2O_3 inclusions. The interfacial energy between Al_2O_3 and Al-HEA under different Al contents was calculated and the corresponding coagulation coefficients are shown in Figure 10(b). As can be seen, the coagulation coefficient of Al_2O_3 inclusions decreases with the increase of Al content, and it is higher than those of spinel inclusions at a lower Al content. This suggests that the coagulation coefficient of the same type of inclusion can change due to the difference in physical parameters of HEA melt and inclusion amount. Experimental validation needs to be performed in future work.

IV. CONCLUSIONS

In the present study, three different $\text{Co}_{47.5}\text{Cr}_{30}\text{Fe}_{7.5}\text{Ni}_{7.5}\text{Mn}_{7.5}$ -based alloys were manufactured by different methods which contained different levels of impurities and Al content. The inclusion characteristics and effect of Al content on inclusion formations were systematically analyzed based on experimental characterization

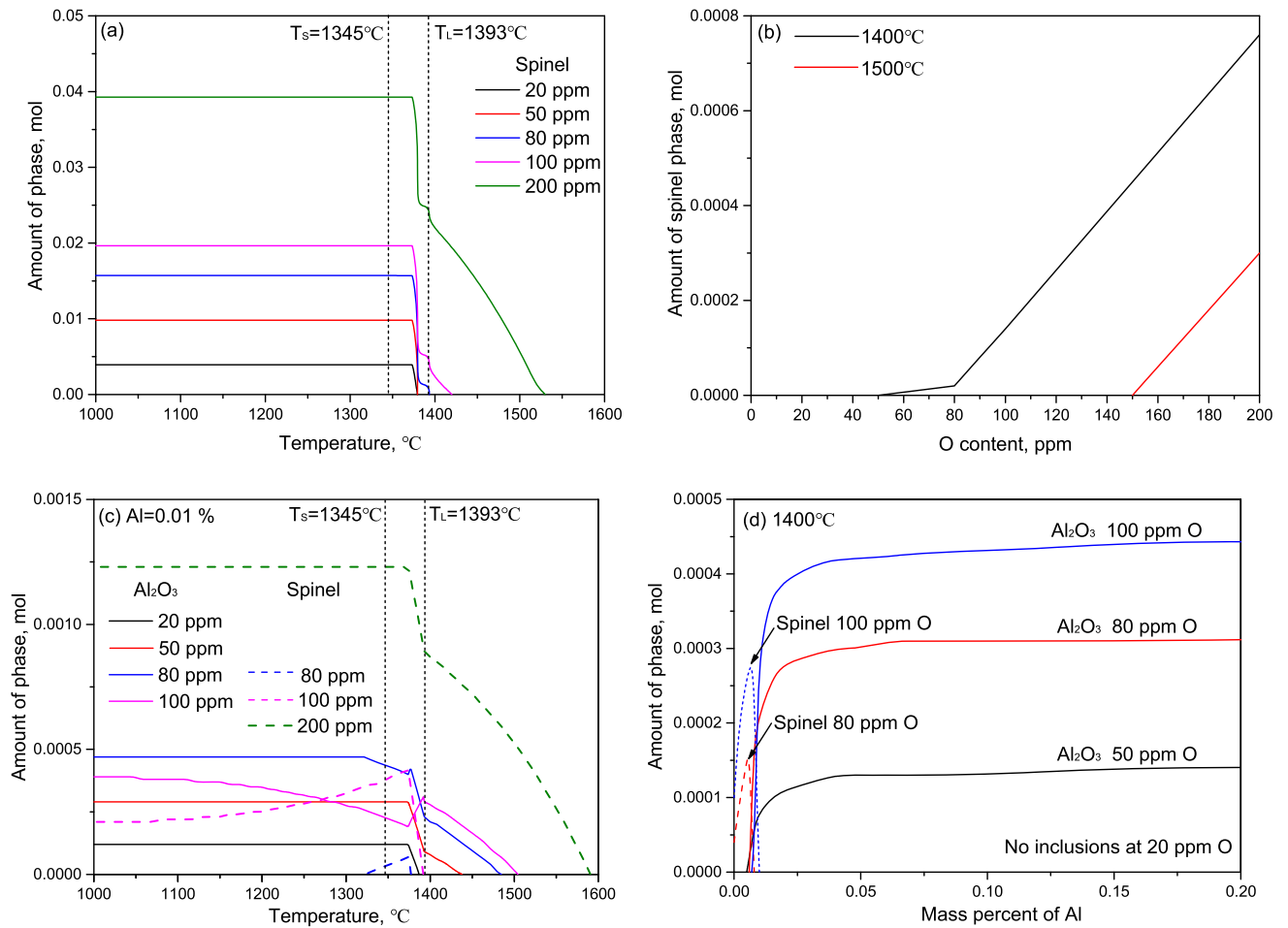


Fig. 9—Effect of oxygen content on the formation of spinel inclusions without considering Al (a, b), spinel and Al_2O_3 inclusions containing different amount of Al (c, d).

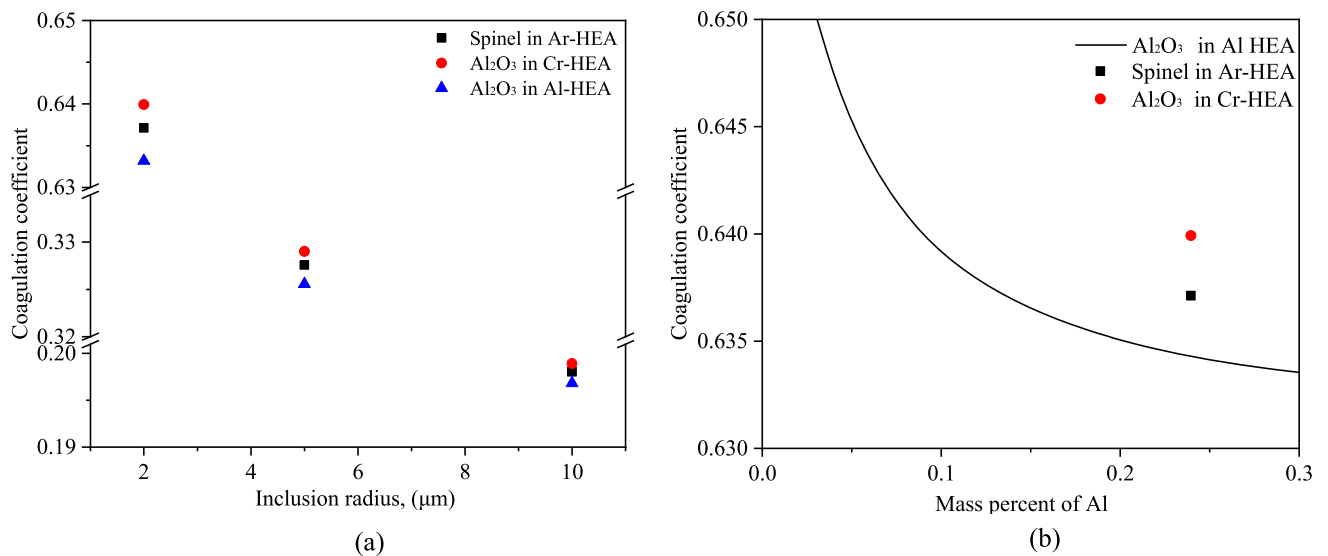


Fig. 10—Coagulation coefficient of different inclusions with the change of (a) inclusion radius, (b) Al content in three HEA samples.

and thermodynamic calculation. The specific conclusions are summarized as follows:

- (1) According to the experimental results, Mn(S,Se) inclusions were found in three HEAs. In terms of oxide inclusions, MnCr_2O_4 inclusions were the representative oxides present in Ar-HEA, Al_2O_3 were the typical inclusions in Cr-HEA, and Al_2O_3 , $\text{Mn}(\text{Cr,Al})_2\text{O}_4$ inclusions were found in Al-HEA.
- (2) Thermodynamic computation predicted $\text{Mn}(\text{Cr,Al})_2\text{O}_4$, Al_2O_3 inclusions can be formed in Al-containing $\text{Co}_{47.5}\text{Cr}_{30}\text{Fe}_{7.5}\text{Ni}_{7.5}\text{Mn}_{7.5}$ HEA. The stable inclusions can transform from MnCr_2O_4 inclusions to $\text{Mn}(\text{Cr,Al})_2\text{O}_4$ inclusions and pure Al_2O_3 inclusions with the increase of Al content. The inclusions in Al-containing HEA are spinel or Al_2O_3 depending on Al and O contents. The formation of spinel and Al_2O_3 inclusions can be avoided in liquid $\text{Co}_{47.5}\text{Cr}_{30}\text{Fe}_{7.5}\text{Ni}_{7.5}\text{Mn}_{7.5}$ -HEA when the O content is less than 50 ppm.
- (3) The calculated coagulation coefficient of spinel inclusions is close to that of Al_2O_3 inclusions. Besides, the coagulation coefficient of Al_2O_3 inclusions can be affected by the Al content in the melt, which can be explained by the different physical parameters between inclusions and HEA matrix.

ACKNOWLEDGMENTS

W. Mu would like to acknowledge the Swedish Foundation for International Cooperation in Research and Higher Education (STINT, Project No. IB2020-8781), VINNOVA (No. 2022-01216) and the Swedish Steel Producers' Association (Jernkontoret), in particular, Axel Ax:son Johnsons forskningsfond, Prytziska fonden nr 2, and Gerhard von Hofstens Stiftelse för Metallurgisk forskning for the financial support. STINT grant (IB2022-9228) & National Excellent Young Scientists Fund (project name: Intelligent Inclusion Metallurgy) are acknowledged by W. Mu and Q. Wang for the research collaboration between KTH and NEU. Y. Wang acknowledges the Key Laboratory for Ferrous Metallurgy and Resources Utilization of Ministry of Education and Hubei Provincial Key Laboratory for New Processes of Ironmaking and Steelmaking (No. FMRUlab-22-1) and College Students' innovation and entrepreneurship training program (S202210488092) for supporting this research. W. Wang would like to acknowledge the funding from a Key R&D item in Science and Technology Development Project and International Collaborative in Science and Technology Development Project, Science and Technology Department of Jilin Province (Grant No. 20200401106GX and 20210402061GH). H. Kong would like to acknowledge

Key Research and Development Plan of Anhui Province (202104b11020007), Anhui special support plan (T000609), and distinguished professor of the Wanjiang Scholars project for the financial support.

CONFLICT OF INTEREST

The authors declare that they have no conflict of interest.

FUNDING

Open access funding provided by Royal Institute of Technology.

OPEN ACCESS

This article is licensed under a Creative Commons Attribution 4.0 International License, which permits use, sharing, adaptation, distribution and reproduction in any medium or format, as long as you give appropriate credit to the original author(s) and the source, provide a link to the Creative Commons licence, and indicate if changes were made. The images or other third party material in this article are included in the article's Creative Commons licence, unless indicated otherwise in a credit line to the material. If material is not included in the article's Creative Commons licence and your intended use is not permitted by statutory regulation or exceeds the permitted use, you will need to obtain permission directly from the copyright holder. To view a copy of this licence, visit <http://creativecommons.org/licenses/by/4.0/>.

REFERENCES

1. J.W. Yeh, S.K. Chen, S.J. Lin, J.Y. Gan, T.S. Chin, T.T. Shun, C.H. Tsau, and S.Y. Chang: *Adv. Eng. Mater.*, 2004, vol. 6, pp. 299–303.
2. B. Cantor, I. Chang, P. Knight, and A. Vincent: *Mater. Sci. Eng. A*, 2004, vol. 375, pp. 213–18.
3. G. Laplanche, A. Kostka, O. Horst, G. Eggeler, and E. George: *Acta Mater.*, 2016, vol. 118, pp. 152–63.
4. F. Otto, A. Dlouhý, C. Somsen, H. Bei, G. Eggeler, and E.P. George: *Acta Mater.*, 2013, vol. 61, pp. 5743–55.
5. F. Otto, N.L. Hanold, and E.P. George: *Intermetallics*, 2014, vol. 54, pp. 39–48.
6. K. Lu, A. Chauhan, D. Litvinov, M. Walter, A.S. Tirunilai, J. Freudenberger, A. Kauffmann, M. Heilmaier, and J. Aktaa: *Mater. Sci. Eng. A*, 2020, vol. 791, 139781.
7. A. Wang, X. An, J. Gu, X. Wang, L. Li, W. Li, M. Song, Q. Duan, Z. Zhang, and X. Liao: *J. Mater. Sci. Technol.*, 2020, vol. 39, pp. 1–6.
8. Z. Xu, H. Zhang, W. Li, A. Mao, L. Wang, G. Song, and Y. He: *Addit. Manuf.*, 2019, vol. 28, pp. 766–71.
9. W. Wang, Y. Wang, W. Mu, J.H. Park, H. Kong, S. Sukenaga, H.

- Shibata, H. Larsson, and H. Mao: *Mater. Des.*, 2021, vol. 210, 110097.
10. N. Choi, K. Lim, Y. Na, U. Glatzel, and J. Park: *J. Alloys Compd.*, 2018, vol. 763, pp. 546–57.
 11. J.J. Licavoli, M.C. Gao, J.S. Sears, P.D. Jablonski, and J.A. Hawk: *J. Mater. Eng. Perform.*, 2015, vol. 24, pp. 3685–98.
 12. B. Gludovatz, E.P. George, and R.O. Ritchie: *JOM*, 2015, vol. 67, pp. 2262–70.
 13. N. Choi, N. Park, J.K. Kim, A.V. Karasev, P.G. Jönsson, and J.H. Park: *Metals*, 2020, vol. 10, p. 1286.
 14. N. Stepanov, N.Y. Yurchenko, D. Shaysultanov, G. Salishchev, and M. Tikhonovsky: *Mater. Sci. TechNOL.*, 2015, vol. 31, pp. 1184–93.
 15. B. Kang, J. Lee, H.J. Ryu, and S.H. Hong: *J. Alloys Compd.*, 2018, vol. 767, pp. 1012–021.
 16. M. Klimova, N. Stepanov, D. Shaysultanov, R. Chernichenko, and S. Zhrebtsov: *Materials*, 2018, vol. 11, p. 53.
 17. M.A. Hemphill, T. Yuan, G.Y. Wang, J.W. Yeh, C.W. Tsai, A. Chuang, and P.K. Liaw: *Acta Mater.*, 2012, vol. 60, pp. 5723–34.
 18. O.N. Senkov, S.V. Senkova, and C. Woodward: *Acta Mater.*, 2014, vol. 68, pp. 214–28.
 19. S.K. Wong, T.T. Shun, C.H. Chang, and C.F. Lee: *Mater. Chem. Phys.*, 2018, vol. 210, pp. 146–51.
 20. B. Kang, T. Kong, H.J. Ryu, and S.H. Hong: *J. Mater. Sci. Technol.*, 2021, vol. 59, pp. 32–41.
 21. E. Holmström, R. Lizarraga, D. Linder, A. Salmasi, W. Wang, B. Kaplan, H. Mao, H. Larsson, and L. Vitos: *Appl. Mater. Today*, 2018, vol. 12, pp. 322–29.
 22. W. Wang, W. Mu, D. Wei, H. Wu, L. Yu, H. Mao, T. Jonsson, and H. Larsson: *Mater. Des.*, 2022, vol. 233, 111166.
 23. W. Wang, W. Mu, Z. Hou, S. Sukenaga, and H. Mao: *Materialia*, 2020, vol. 14, 100928.
 24. W. Mu, Michelic, S.K. and Q. Wang: *Front. Mater.*, 2022, vol. 9, 922203.
 25. A. Karasev, Y. Bi, and P. Jönsson: AISTech-2013, in *Proceedings of the Iron and Steel Technology Conference*, 2013, pp. 1–7.
 26. K. Oikawa, H. Ohtani, K. Ishida, and T. Nishizawa: *ISIJ Int.*, 1995, vol. 35, pp. 402–08.
 27. J.L. Lu, G.G. Cheng, L. Chen, G.J. Xiong, and L.S. Wang: *ISIJ Int.*, 2018, vol. 58, pp. 1307–15.
 28. L.C. Zheng, A. Malfliet, P. Wollants, B. Blanpain, and M.X. Guo: *ISIJ Int.*, 2016, vol. 56, pp. 1529–36.
 29. L.C. Zheng, A. Malfliet, P. Wollants, B. Blanpain, and M.X. Guo: *Metall. Mater. Trans. B*, 2017, vol. 48B, pp. 2447–58.
 30. Y. Wang, A. Karasev, and P.G. Jönsson: *Steel Res. Int.*, 2020, vol. 91, p. 1900669.
 31. J.O. Andersson, T. Helander, L. Hglund, P. Shi, and S. Bo: *Calphad*, 2002, vol. 26, pp. 273–312.
 32. Thermo-Calc Software: TCS Steels/Fe-Alloys Database Version 11.0 (TCFE11), Stockholm, December 2020.
 33. M.H. Lee and J.H. Park: *Metall. Mater. Trans. B.*, 2018, vol. 49B, pp. 877–93.
 34. B.V.R. Chowdari, H.L. Yoo, G.M. Choi, and J.H. Lee: *Solid State Ionics: The Science and Technology of Ions in Motion*, World Scientific, Singapore, 2004.
 35. K. Nakajima, W. Mu, and P.G. Jönsson: *Metall. Mater. Trans. B.*, 2019, vol. 50B, pp. 2229–37.

Publisher's Note Springer Nature remains neutral with regard to jurisdictional claims in published maps and institutional affiliations.